1   **Title:**

2   **Cross-borehole geoelectrical time-lapse monitoring of in-situ chemical oxidation and**

3   **permeability estimation through induced polarization**

4

5   **Running Title:**

6   **Time-lapse ISCO monitoring and IP permeability**

7

8   **Author list:**

9

10   Thue Bording[1] (bording@geo.au.dk)

11   Anders Kristian Kühl [1][T](anders.kuhl@geo.au.dk)

12   Gianluca Fiandaca[1][2] (gianluca.fiandaca@unimi.it)

13   Jørgen Fjeldsø Christensen[3] (Joergen.F.Christensen@regionsyddanmark.dk)

14   Anders Vest Christiansen[1](anders.vest@geo.au.dk)

15   Esben Auken[1](esben.auken@geo.au.dk)

16

17   [1] HydroGeophysics Group, Department of Geoscience, Aarhus University, Denmark

18   [2] Dipartimento di Scienze della Terra "A. Desio", Università degli Studi di Milano, Italy

19   [3] Region of Southern Denmark

20   [T] Corresponding author: HydroGeophysics Group, Department of Geoscience, Aarhus
21   University, Building 1120, C.F. Møllers Alle 4, 8000 Aarhus C, Denmark

22

23

24

25

26

27

28

Abstract

Worldwide, soil contamination due to industrial activities is a major issue. One method for remediation of contaminated sites is in-situ chemical oxidation, where an oxidizing agent is injected into the contaminated soil. Normally, monitoring wells are established in the remediation area for tracking the oxidizing agent. However, wells only provide point information of the injectant spread. This issue can be addressd by cross-borehole resistivity and induced polarization (IP) tomography, by mapping the electrical properties in the entire remediation volume and by deriving, thorugh petrophysical relations, the hydraulic properties of the medium. Here we present a proof of concept study, performed over one year as part of a larger remediation project, where resistivity and time-domain IP data were acquired among 10 boreholes, before and after two rounds of injection of oxidizing agents. The time-lapse resistivity models, obtained through a focusing inversion scheme that favours compact time-lapse changes, clearly show the oxidizing agent spread as highly conductive anomalies, and confirmed by water conductivity measurements in boreholes. The time-lapse inversions also show spatial variability in the injectant spread, with some areas not reached. The IP data quality decreased significantly just after the injection rounds, because of the decrease in resistivity and IP signal level, so that IP time-lapse inversions were not feasible. However, the IP data were used for background characterization, and to estimate permeability. In particular, there is a good match between the imaged low-permeability zones and the areas in which the injectant did not spread, identified by the time-lapse resistivity inversions. Furthermore, geological samples confirm the presence of fine-grained sediments in the estimated low-permeability zones. While time-lapse resistivity tomography may be used for documenting the injectant spread, IP permeability estimates prior to injection can be used to better tailor the remediation in terms of dimension and location of injection filters.

Keywords: Electrical Resistivity Tomography, Cross-borehole, Time-lapse monitoring, Permeability

54

Acknowledgements

60

Data availability statement

Data available on request from the authors: The data that support the findings of this study are available from the corresponding author upon reasonable request.

64

Introduction

Soil contamination due to past industrial activities has become a major issue in urban and natural areas worldwide. Contamination can be found on the grounds of former and current dry cleaners, gas stations and chemical factories, as well as in the landfills that received waste from such sites. In Denmark alone, over 10.000 of these sites have been identified, with ten sites having been designated as "Generational Contaminations". These are large and complex polluted sites which pose an active risk for either the groundwater or the environment, and are expected to be problematic for generations to come if no actions are taken.

One way of addressing these contaminated sites is with in-situ chemical remediation, where a remediation agent is injected into the contaminated soil, in order to break down the pollutants (Tsitonaki et al., 2010). One of the main issues with this type of remediation strategy is ensuring that the injectant spreads throughout the entire targeted volume (Pac et al., 2019). Traditionally this is verified from a number of monitoring wells with samples taken for chemical analysis in order to determine whether the injectant has reached the well or not. However, this approach does not provide any direct information on the spread of the remediation material between the monitoring wells, as it is limited by the positions of the wells and the screen sizes. As the geology of the targeted volume can often be complex, it can lead to false assumptions on the real spread of the remediation material. This can easily be the case in Danish glacial and postglacial deposits, where sand bodies can be found within clays and vice versa. The resulting large variations in permeability between the different lithologies then lead to inhomogeneous flow paths for the injectant.

Cross-borehole electrical resistivity tomography provides a possible method for mapping the spread of the injected remediation material between the observation wells when the injectant has a considerable difference in conductivity to the native pore-fluid. Resistivity mapping could also be accomplished through surface measurements, but for these the vertical resolution inevitably

90   decreases with depth. The cross-borehole approach allows for a high, constant vertical resolution

91   throughout the volume of interest, given appropriately spaced boreholes and borehole electrodes.

92   The usefulness of cross-borehole resistivity tomography has been demonstrated for various

93   purposes, such as the characterization of hydrogeological properties of the vadose zone (Binley

94   et al., 2002; Looms et al., 2008a), monitoring of unsaturated flow and transport (Looms et al.,

95   2008b), characterization of solute transport by use of saline tracer tests (Perri et al., 2012; Slater

96   et al., 2000), the monitoring of remediation (LaBrecque et al., 1996; Mao et al., 2016; Mao et al.,

97   2015) and mapping of possible contaminant flow-paths (Bording et al., 2019).

98   Increasingly, IP measurements are included in resistivity measurement campaigns. The IP data

99   can add complementary information for the characterization of the subsurface (Kemna et al.,

100   2004) and can be measured in both the frequency domain (FD) or in the time domain (TD), see

101   Maurya, et al. (2018b) for an in depth comparison of the strengths and limitations of both methods

102   for field surveys. FDIP has been used in a number of environmental and remediation studies for

103   monitoring progress and changes to the remediation effort. In many applications it has been shown

104   that the FDIP data can be used in the continual monitoring of activity of in-situ bioremediation

105   (eg. Chen et al., 2012; Commer et al., 2011; Orozco et al., 2013; Orozco et al., 2011) and

106   monitoring chemical remediation through injection of micro to nanoscale iron (eg. Flores Orozco

107   et al., 2019; Flores Orozco et al., 2015; Slater and Binley, 2006a).

108   One of the earliest applications of IP measurements in the cross-borehole case, was the frequency

109   domain IP study presented in Kemna, et al. (2004) where the target was to image hydrocarbon

110   contamination and the lithologies present, as well as to estimate permeability at different

111   contaminated sites. An early use of FDIP in cross-borehole, was for monitoring the integrity of a

112   permeable reactive barrier (Slater and Binley, 2003, 2006a).

113   The TDIP method, which allows for acquiring the IP data simultaneously with the resistivity data,

114   has been used in cross-borehole applications since the early days (Slater and Binley, 2006b), and

115   has recently seen increasing use. Binley, et al. (2016) presented a TDIP study, where the goal was

116 a hydrogeological characterization and permeability estimation of the unconsolidated sediments.

117 Here they used the integral chargeability measurement, disregarding the spectral content present

118 in the IP data. Similarly, Aristeidis, et al. (2019) used TDIP measurements for characterization of

119 remediation efforts, but only used integral chargeability. In Bording, et al. (2019) the first

120 application of full-decay spectral TDIP in cross-borehole configurations was presented for the

121 mapping of finer sand structures in a glacial till deposit.

122 In surface applications, full decay spectral TDIP has been used in a number of different studies,

123 such as for the characterization of landfills and contaminated sites (Gazoty et al., 2012a;

124 Johansson et al., 2015; Wemegah et al., 2017), lithological discrimination (Gazoty et al., 2012b;

125 Rossi et al., 2017), time-lapse monitoring of CO_2 injections (Doetsch et al., 2015a; Fiandaca et

126 al., 2015) and active layer dynamics (Doetsch et al., 2015b) and, more recently, for permeability

127 estimation (Fiandaca et al., 2018c; Maurya et al., 2018a).

128 In this study, we present the application of cross-borehole resistivity and full-decay spectral TDIP

129 tomography in a remediation project, with the aim of mapping the spread of a conductive

130 oxidizing agent (persulfate activated by hydrogen peroxide) through time-lapse measurements,

131 and of extracting reliable information from the IP data, both for inferring possible effects of the

132 contamination on the IP properties, and for estimating permeability. In particular, the study was

133 performed in Kaergaard Plantation, shown in blue on Figure 1a, one of the largest contaminated

134 sites in Denmark, in which two rounds of injection of oxidizing agent were carried out in 2018,

135 together with water and soil geochemical samplings and with six rounds of TDIP measurements

136 over 10 electrode boreholes.

137 The oxidizing agent is often, as in this study, highly conductive, which results in a conductive

138 anomaly with strong contrast where the agent is present. In order to avoid too smooth variations

139 in the high-contrast time-lapse inversion models due to regularization, we used the asymmetric

140 generalized minimum support (AGMS) norm developed by Fiandaca et al. (2015) for the time-

141 lapse constraints. This norm favours compact time-lapse changes and it significantly improves

142 the size, shape and magnitude estimates of the time-lapse changes. Unfortunately, the signal level

143 of the TDIP data decreased significantly during the injection rounds because of the high

144 conductivity of the oxidizing agent. This caused the IP signals to become too noisy just after the

145 injection rounds, which means that these IP data sets are not used for time-lapse inversions.

146 However, the IP data collected before injections are used for characterizing the electrical

147 properties of the site before remediation and for estimating permeability. The permeability

148 estimation is carried out following the approach of Fiandaca et al. (2018c) and Maurya et al.

149 (2018a), which applies the empirical petrophysical relations developed by Weller et al. (2015) on

150 the inversion parameters retrieved from a full-decay spectral TDIP inversion. The choice of using

151 the AGMS time-lapse approach and the full-decay spectral IP inversion restricted the choice of

152 the inversion algorithm to 2D cross-borehole inversions. These are carried out following Fiandaca

153 et al. (2013) and Bording et al. (2019) with the AarhusInv inversion algorithm (Auken et al.,

154 2015), because these approaches are not available in 3D inversion algorithms (eg. Binley et al.,

155 2016; Commer et al., 2011; Günther and Rücker, 2012; Karaoulis et al., 2013; Loke et al., 2014).

156 It is however not without limitations to use a 2D inversion where 3D effects are to be expected.

157 The appropriateness and limitations of this 2D approach will be discussed in detail in the result

158 and discussion sections.

159

160 **Site description**

161 Geological setting
162 The site is located in western Jutland, Denmark, in between sand dunes and 600 m from the coast.

163 It was formed postglacially as part of a barrier coast, with a complex system of inlets, barrier-

164 islands, lagoons and tidal inlets. This has resulted in a varied deposition of permeable sands and

165 gravels, as well as occasional silts and clays. These coarser materials were deposited in higher

166 energy regimes such as channels, while the finer materials were deposited when cut off from the

167 ocean, such as by a coastal barrier. This environment means that there can be lateral and vertical

168 variabilities in hydraulic conductivity in the area, which may influence both the distribution of

169 present contaminants and the transport of the injected material. At a depth of 20-25 m a clayey-

170 silt layer underlies the site. This layer has not been penetrated by boreholes, as it is thought to be

171 impermeable to the pollution, and it might result in contamination of deeper groundwater

172 (Arbejdsgruppen vedrørende Kærgård Plantage, 2006). A geological description based on core

173 samples is available from borehole B809 in the elevation interval 2.8 m to -0.2 m, showing fine-

174 grained sand in the top, coarsening downwards alternating between coarse sands and gravel.

Contamination

176 In the period between 1956 to 1973, daily tank truck deliveries with farmaceutical wastewater

177 from Grindstedværket, seen in red on Figure 1a, were deposited in Kaergaard Plantation in six

178 separate pits. In total, an estimated 286,000 m^3 of wastewater was dumped at the site. The

179 resulting groundwater contamination includes both dense and light non-aqueous phase liquids, in

180 the form of sulfonamides, barbiturates, benzene and chlorinated solvents and poses a health risk

181 to humans and local wildlife. Due to the contamination leaching from the groundwater into the

182 ocean, a bathing ban has been imposed along a 1400 m stretch of the coast (Arbejdsgruppen

183 vedrørende Kærgård Plantage, 2005). An airborne TEM survey over the site in Kaergaard

184 Plantation (Christensen and Halkjær, 2014) showed that the average resistivity in the area was

185 around 200 Ωm, with a conductive plume found in elevations -10 m to -20 m relative to sea level,

186 with resistivity values around 5-10 Ωm and lower, possibly due to presence of degradation

187 products.

Remediation

189 Remediation of the site was carried out in several phases. Between 2007 and 2015, over 7500

190 tons of toxic sludge were excavated from the surfaces of pits 1 through 4. This sludge was then

191 transported and thermally treated in Germany and the Netherlands, and thus the upper 3 m of the

192 pits were replaced with fine sands, to prevent any immediate contact between the remaining

193 pollution and the surface. At the same time, the Region of Southern Denmark completed a

194 technology development project, which showed that a chemical primary treatment followed by a

195 secondary biological treatment would be the most efficient method to clean the contamination

196 affecting the groundwater in the area.

197 The chemical treatment uses persulfate activated by hydrogen peroxide, which releases free

198 radicals that oxidize the bulk of the contamination (Tsitonaki et al., 2010). Following the chemical

199 treatment, the secondary biological treatment consists of adding Dehalococcoide bacteria, a

200 natural soil bacterium which can break down the remaining chlorinated solvents in the soil

201 (Region of Southern Denmark, personal communication).

202 The second phase of the remediation began in 2017, where pit 3 was chosen as the first site for

203 cleanup using the chosen procedure. The chemical treatments were applied by injecting the

204 oxidizing agent in a dense hexagonal grid of injection wells covering ~1000 m^2 with 3 m between

205 each injection point. In total 126 injection points were established across the pit, with each point

206 consisting of two boreholes directly adjacent to each other with filters at two different depths. The

207 injections were performed between elevations 3 m and 0 m in two separate filters placed at

208 elevations 3 m to 1.5 m and 1.5 m to 0 m. Throughout the remediation process, a geochemical

209 monitoring was performed by use of several monitoring wells established in the pit. The location

210 of all boreholes in pit 3 and their purpose can be seen in Figure 1b.

211 Monitoring wells for geochemistry

212 Thirty-three wells were established in pit 3 for monitoring geochemistry. Twenty-four of the

213 monitoring wells have two filters at elevations 2.8 m to 1.3 m and 1.3 m to -0.2 m, while the

214 remaining nine monitoring wells have three filters, of which only the uppermost ranging from

215 elevation 2.8 m to -1.2 m is in our interest. Two monitoring boreholes, one of each type, are

216 located inside the study area, i.e. B870 and B809. The geochemical data collected in the wells,

217 together with analyses of soil samples collected at/close to B809 before/after the injection rounds

218 are presented in the methodology section.

219 Monitoring wells are typically used both to evaluate the spread of the oxidizing agent and the

220 degradation of contaminants, but the information that can be achieved with monitoring wells

221 comes with two major limitations: limited lateral resolution and limited vertical resolution (Pac

222 et al., 2019). The vertical resolution of the monitoring wells is limited by the number and lengths

223 of filters, with large filters averaging large volumes, making it impossible to tell if the oxidizing

224 agent is present in the entire interval or just a part of it. The lateral resolution is limited by the

225 number and spatial distribution of the monitoring wells. Looking at Figure 1b, it is also clear that

226 the majority of the area investigated in this study does not have a monitoring borehole in the

227 immediate vicinity.

Methodology

229 Geophysical survey layout, Data Acquisition and Processing

230 The measurement setup in the field consisted of ten electrode boreholes, placed within an 55 m^2

231 area, see Figure 1b and 1c. The electrode-tubes installed in the boreholes had 32 electrodes with

232 an electrode spacing of 25 cm. The electrode tubes were made by clamping a 2 cm acid resistant,

233 stainless steel ring onto the 32 mm PVC-tubes. Individual wires were soldered onto the metal

234 rings, led along the tube and finally joined in a 32-pin connector.

235 A 12 channel ABEM Terrameter LS was used to perform the TDIP measurements. A 100% duty

236 cycle waveform was used with 2 seconds on-time (Olsson et al., 2015). Three array types were

237 used in acquiring the measurements: a) collinear dipole-dipole single borehole measurements, b)

238 parallel cross-borehole dipole-dipole arrays, c) equatorial cross-borehole dipole-dipole arrays,

239 these are described in detail in Bording, et al. (2019). The measurement sequence was optimized

240 to maximize the time between electrodes being used as potential after have been used as current

241 electrodes, to minimize effects of electrode polarization.

242 The electrodes were installed in February 2018 and data were subsequently acquired in six rounds

243 during 2018-2019, of which there were two rounds of injections, see Table 1. During each

244 measurement round, nine different configurations were measured, each consisting of three

245 electrode-boreholes, see the line segments in Figure 1c. Table 1 also shows the number of

246 quadrupoles measured for each round. The acquisition time was 12-18 hours for each round

247 depending on the number of quadrupoles measured. The variation in the number of acquired data

248 is mainly due to changes in contact resistance above the groundwater table, as electrodes with

249 contact resistances above a cutoff criterion of 20 kΩ were not used. As an example of the contact

250 resistance, Figure 2a shows the contact resistances measured in borehole 5 for the two injection

251 rounds, while Figure 2b shows the contact resistances for non-injection rounds. The electrode

252 resistance was high in the unsaturated zone, in the tens of kΩ, but beneath this, contact resistances

253 decreased, to a few kΩ. It is also seen in Figure 2a that the contact resistances drop down to a few

254 hundreds of Ω, for a large fraction of the electrodes in round 3 and 5. This is immediately after

255 the injection, and is a clear indication of the injectant approaching the electrodes. The cutoff

256 criteria of 20 kΩ for omitting electrodes in the measurements is also seen in red in Figure 2,

257 showing that most of the deactivated electrodes are in the upper 2 m, and that the number of

258 electrodes with high contact resistance varies between the different measurement rounds.

259 The full waveform data were signal-processed following the methodology described by Olsson,

260 et al. (2016) with harmonic de-noising, drift correction and spike removal. Following the signal

261 processing,   the   IP   data   were   imported   to   the   Aarhus   Workbench   software

262 (www.aarhusgeosoftware.dk), where a manual processing of the IP decay curves was performed,

263 where erratic or negative decays were removed, along with gates deviating from otherwise smooth

264 decays. The main issues were high contact resistance for some of the electrodes, capacitive

265 coupling, and poor signal to noise ratio in general. In general, the quality of the IP data was not

266 high so a large fraction of the data had to be removed. In the measurements rounds directly after

267 injections, the highly increased conductivity further decreased the signal to noise ratio and the

268 quality of the IP data. Figure 3 presents the comparison on selected representative quadrupoles of

269 the IP decays before and after the first round of injection (i.e. acquisition rounds 1 and 3), where

270 it is clearly visible that the IP data quality decreases significantly just after the injection, due to

271   the decrease in resistivity values, and consequently in the IP voltage level: IP data just after the

272   injection rounds cannot be used for inversion.

273   Water and soil samples

274   In-field measurements in the monitoring wells consisted of water conductivity, pH, Redox

275   potential and temperature, while lab analyses were carried out for a range of chemical components

276   of which we have included PCE and total sum of hydrocarbons. The water chemistry available

277   within the study area is presented in Table 2. In particular, the water conductivity measured in the

278   filters and shown in Table 2 will be used for comparison to the geophysical imaging in the result

279   section. Unfortunately, the monitoring program did not measure water conductivity in boreholes

280   B809 and B870 prior to the injections, so there are no baseline values for the water conductivity.

281   In borehole B809, soil samples were collected prior to the first injection round. After the second

282   injection round and immediately adjacent to B809, a new set of soil samples were collected. The

283   samples were analysed for a range of chemical compounds, of which we present PCE and total

284   sum of hydrocarbons in Table 3. Prior to the remediation, the highest concentrations were found

285   at elevation 2.3 m.

286   Inversion

287   The collected data were inverted using two different approaches, all within the framework of

288   AarhusInv (Auken et al., 2015). The first approach is an L_2 time-domain IP inversion used for

289   background and permeability estimation. The second approach is time-lapse inversions of

290   resistivity to map conductive anomalies. The time-domain IP forward responses were calculated

291   as described in Fiandaca, et al. (2013), with a modification for buried electrodes used in Bording

292   et al. (2019). When calculating the forward response, it is assumed that the 2D model extends

293   indefinitely perpendicularly to the measured profile, with the electrodes modelled as points. The

294   inversions were performed along intersecting profiles and compared to identify the effect of

295   possible 3D-structures on the models in the vicinity of the intersections. The inversions were

296   carried out on a regular grid consisting of 81 x 25 cells, with cells dimensions 12.5 cm x 50 cm

297   (thickness x width) and standard smooth (L₂) horizontal and vertical constraints. The horizontal

298   constraints were set to 1.075, which is the standard deviation factor of the roughness covariance

299   matrix in the objective function; similarly, the vertical constraints were set to 1.1.

300   The time-lapse inversions were performed following the framework of (Fiandaca et al., 2015).

301   This inversion scheme uses an iteratively reweighted least-squares (IRLS) approach, which

302   allows for using norms in the time-lapse constraints different from the standard L₂ least-squares

303   norm. In particular, the asymmetric generalized minimum support norm (AGMS) proposed by

304   Fiandaca et al. (2015) was used for the time-lapse constraints. The AGMS norm penalizes all the

305   time-lapse variations over the given threshold σ of the parameter variations (5% in the inversions

306   presented here), regardless of the magnitude of the variation itself. In this way, big parameter

307   variations are not over-penalized, avoiding the too smooth variations in the time-lapse inversion

308   models that might occur when using the classic L₂ time-lapse norm. The AGMS norm depends

309   on a second setting, i.e. the expected relative area/volume of time-lapse changes α, which controls

310   the relative weight of data and model penalizations in the objective function. The same value

311   α=0.2 was used when inverting all acquisition rounds against the background model, chosen as

312   the model retrieved form the data of the first acquisition round.

313   In this study, the spectral IP content was parameterized using the maximum phase angle (MPA)

314   model from Fiandaca, et al. (2018a), which is a re-parameterization of the Cole-Cole model (Cole

315   and Cole, 1941). The Cole-Cole model in its complex resistivity form is given as (Pelton et al.,

316   1978):

317    $\rho^*(\omega) = \rho_0 \left[1 - m_0 \left(1 - \frac{1}{1+(i\omega\tau_\rho)^c} \right) \right],$ (1)

318   Where ρ^* is the complex resistivity, ω is the angular frequency, ρ_0 is the DC resistivity, m_0 is

319   the intrinsic chargeability, τ_ρ is the time constant, C is the frequency exponent and i is the

320   imaginary unit. The MPA re-parameterization is then defined by the parameters:

321 $$\boldsymbol{m_{MPA}} = \{\rho_0, \varphi_{max}, \tau_\varphi, C\}, \tag{2}$$

322 Where φ_{max} is the maximum of the Cole-Cole phase spectrum, which substitutes m_0, and τ_φ is

323 the inverse of the frequency at which the phase peak is reached. The IP inversions were performed

324 with the same grid and roughness constraints as the time-lapse resistivity inversions. The MPA

325 re-parameterization was used, instead of the classic Cole-Cole model, as its parameters are less

326 correlated, resulting in better determined inversion parameters. The Cole-Cole like spectral model

327 was chosen because it allows an acceptable fit to the IP decays, contrary to for example the

328 Constant Phase Angle Model (Johansson et al., 2015; Van Voorhis et al., 1973) which gives an

329 almost doubled data fit.

330 Permeability estimation
331 The permeability estimation in Fiandaca et al. (2018c) and Maurya et al. (2018a) is based on the

332 empirical petrophysical relations that link electrical properties and permeability, as derived from

333 laboratory data by Weller et al. (2015) for unconsolidated samples:

334 $$k = \frac{1.08 \cdot 10^{-13}}{F^{1.12} \cdot \sigma''^{2.27}} \tag{3a}$$

335 $$k = 3.47 \cdot 10^{-16} \cdot \frac{\sigma_0^{1.11}}{\sigma''^{2.41}} \tag{3b}$$

336 Equations (3a) and (3b) were found practically equivalent by Weller et al. (2015), and link the

337 permeability k to the formation factor F and the imaginary conductivity σ'' (equation 3a) or to

338 the DC conductivity σ_0 and the imaginary conductivity σ'' (equation 3b), for samples prepared

339 with a standardized solution of NaCl with electrical conductivity equal to 100 mS/m.

340 In Fiandaca et al. (2018c) and Maurya et al. (2018a) equation (3a) was used for permeability

341 estimation, because the Cole-Cole model was re-parameterized with the Bulk and Imaginary

342 Conductivity (BIC) model, which is described by the bulk conductivity $\sigma_{bulk} = \sigma_0 - \sigma'_{surf}(\omega =$

343 $0)$, the maximum imaginary conductivity σ_{max}, the time constant τ_σ and the frequency exponent

344 C. The permeability in this study is computed through equation (3b), deriving the imaginary

345 conductivity as $\sigma'' = {\varphi_{max}}/{\rho_0}$.

346 No correction for water conductivity was carried out when applying equation (3b), because the

347 total dependence on water conductivity of equation (3b) through σ_0 and σ'' almost cancel out

348 because of the exponent present in the formula (Fiandaca et al., 2018b).

349

350 # Results

351 Time-lapse resistivity-only inversions
352 The results of the time-lapse inversions of resistivity of measurement rounds 2, 3 and 4, for the

353 lines E02_E05_E08 and E03_E05_E07 are shown in Figure 4 and 5, respectively, as resistivity

354 sections and resistivity-ratio plots. The relative positions of the two profiles are seen in Figure 1c

355 where they are marked in yellow, and they overlap at the central electrode borehole E05. The

356 dates of the measurement rounds can be seen in Table 1, and correspond to before, immediately

357 after, and several months after injections. Figure 4 and 5 also show the used electrodes in the

358 corresponding rounds, as black dots on the electrode tube, and the position of the injection filters

359 relative to the electrode tubes. Figure 6 shows mean interval resistivity maps and mean interval

360 resistivity-ratio plots for a selection of intervals. These maps are created in two steps: firstly, by

361 computing the geometric average of the resistivity from the inversion models in the vertical

362 direction, every 0.5 m; secondly, interpolating with cubic splines the geometric averages of all

363 the acquisition lines of Figure 1 in the xy plane. These mean interval resistivity maps show no

364 significant artifacts along the 2D inversion lines, with smooth xy features both in the resistivity

365 and resistivity-ratio images. This partly justifies, *a posteriori*, the use of 2D inversions in this

366 study, because no significant resistivity contrasts are present in the xy plane.

367 Both vertical profiles more or less show the same background resistivity, as measured in rounds

368 1 and 2. A highly resistive layer >1000 Ωm, is seen from the surface to elevation 3.5-3.6 m, which

369 corresponds to the unsaturated zone. Between elevations 3.5 m to 2 m, a discontinuous area of

370 lower resistivity (50-80 Ωm) is seen. Within this area, the soils with higher concentrations of

371 contaminants were sampled before the first injection round (Table 3). Below this elevation, the

372 section is comprised mainly of high resistivity (>250 Ωm), with smaller lenses of lower resistivity

373 (80-100 Ωm). The results from the two profiles match up at their cross-over point, even though

374 they were measured and inverted separately, as can be seen also in Figure 6, which is derived

375 from the 2D inversion models retrieved from the ten electrode boreholes.

376 In Figure 4b, measured immediately after the injection along line E02_E05_E08, a large

377 conductive (<10 Ωm) area is observed in the interval from elevation 2 m to -1.2 m. This body

378 overprints the lenses of lower resistivity seen before, but the outline of the lower resistive body

379 between elevation 3.5 m to 2 m is still visible. Figure 4c shows the resistivity measured 2 months

380 after injection, where the resistivity is largely in the same range as before. However, some

381 differences are present, e.g. around elevation 3.5 m, where it is slightly more conductive. Figures

382 5a-c show a similar story for line E03_E05_E07.

383 Figure 4d-f and Figure 5d-f show ratio-plots of time-lapse inversion results, compared to the

384 reference model from round 1. Figure 4d show that no significant changes happened between

385 rounds 1 and 2, which was also expected. Figure 4e shows that the main changes to occur in round

386 3 is the highly conductive anomaly, between elevations 2 m and -1.2 m with resistivities being a

387 factor of 5-100 times lower than the background measurement. It is notable that this anomaly in

388 both Figure 4e and 5e is most pronounced in the elevation interval between 2-1.5 m to 0 m, with

389 the top border being relatively sharply defined, while the bottom border is less defined. This is

390 most pronounced in profile E03_E05_E07 in Figure 5e, while profile E02_05_08 in Figure 4e

391 exhibits more lateral variation. For use in later comparisons, magenta lines have been drawn

392 around the extent of the conductive anomaly in Figure 5e. The lower-contrast differences between

393 round 1 and round 4 are clearly visible in Figures 4f and 5f, and are a combined result of seasonal

394 variations, saturation and, possibly, of the remediation process. However, these lower-contrast

395   differences are not the focus of this study. Overall, the time-lapse inversions using the AGMS

396   focusing scheme retrieves sharp time-lapse resistivity contrasts, without significant smearing due

397   to the time-lapse regularization even when high contrasts are present.

398   Water conductivity was measured in rounds 3 and 4 (Table 2), and the corresponding bulk

399   resistivity values were calculated assuming a formation factor of 4, a commonly use formation

400   factor for sandy sediments. The calculated bulk resistivity values are plotted on Figures 4b-c and

401   5b-c, agreeing fairly well with the resistivities from the inversions, considering that the actual

402   formation factor is unknown. Since no water conductivity measurements exist from the baseline

403   at round 1, in Figures 4e and 5e we show water conductivity ratio between rounds 3 and 4, but

404   with colorscale flipped, to match the resistivity ratios. Also in this case there is a good agreement

405   between the water conductivity contrasts and resistivity-ratios imaged by the time-lapse

406   inversions. This is evidence of the time-lapse inversions depicting the spread of the injectant, due

407   to its low conductivity values.

408   ## IP Inversion and permeability estimation
409   The IP data collected in the first measurement round before any injections, were inverted using

410   the MPA parameterization. We present the inversion of the section E03_E05_E07 in Figure 7.

411   Figure 7a-d show ρ, ϕ_{max}, τ_ϕ and C, in that order from top to bottom, with the outline of the

412   conductive anomaly from Figure 5e marked with a magenta line. The resistivity section is very

413   similar to the resistivity-only time-lapse inversion of round 2 with the same overall structure.

414   ϕ_{max} values are relatively high (>10 mrad) in the unsaturated zone above 3.5 m elevation. Further

415   below, the values decrease, and are generally within the range 0.5-1 mrad, with zones of lower

416   ϕ_{max} present at elevations 2 m and 0 m. Contrary to what was seen in Kemna et al. (2004) no

417   increased ϕ_{max} values are evident at the depths where the most contaminated soils were sampled

418   (i.e. around elevation 2.3 m, see Table 3). This finding might make it less risky to compute the

419   permeability from the IP parameters, under the assumption that the contamination has negligible

420   effects on IP, despite of its high values.

421 The τ_ϕ section seen in Figure 7c shows two anomalies (>1 s) near borehole E3 at elevations 5

422 and 3 m. Below the groundwater table, the values are around 0.03 s to 0.3 s. The C section seen

423 in Figure 7d shows values of 0.6 in the majority of the zone, with one zone of lower values down

424 to 0.3, between boreholes E03 and E05 at elevation 1 m. The high C values ensure that the

425 resolution on the time constant τ_ϕ is higher (Madsen et al., 2017).

426 The permeability estimation, derived from equation (3b) through the inversion parameters ρ and

427 ϕ_{max}, is shown in Figure 7e, along with the position of the injection filters, the outline of the

428 conductive anomaly from round 3, and the geological description from borehole B809. In the

429 unsaturated zone, from the surface to around elevation 3.5 m the estimated permeability is

430 relatively low, $(10^{-11} - 10^{-10}$ m$^2)$, but the permeability estimations have limited validity in the

431 unsaturated zone because full saturation is assumed in equation (3b). The same level of

432 permeability is however seen from below the groundwater table to around elevation 2.5 m. Below

433 this, the permeability is higher by one to two orders of magnitude, albeit with some variation. The

434 upper boundary between high and low permeability align very well with a geological transition

435 from fine to coarse grained sand seen in borehole B809. Consequently, the spatial distribution of

436 the oxidizing agent as determined by the conductive anomaly, may be explained, with due caution

437 because of the high concentrations of contaminants, by the permeability field derived from IP.

438 This would be much more difficult to identify from the resistivity sections only, where the low

439 resistivity areas depend both on the geology and on the water conductivity. In contrast, according

440 to Fiandaca et al. (2018b) and the references therein, the variablity in water conductivity should

441 have a minor effect on the IP-derived permeability estimation.

Discussion

443 The main goal of this study was to assess the usefulness of cross-borehole TDIP in tracking the

444 spread of the injected oxidizing agent in the saturated zone. The injectant used in this case had a

445 strong conductivity contrast in respect to the present pore fluid, and its effect was clear in the

446   initial contact resistances and the overall resistivity measurements and inversions. The time-lapse

447   inversion results clearly showed the range and distribution of the injectant, which was visible as

448   a clear conductive anomaly, and the extent of the oxidizing agent was backed up by water

449   conductivity measurements in the available filters. In the resistivity sections from round 3 in

450   Figure 4b,e and Figure 5b,e, it is seen that the upper boundary of the conductive anomaly cuts the

451   midpoint of the upper filter in borehole B870 and at the midpoint of the upper injection filter in

452   injection wells I102 and I108. Looking only at water conductivity and chemistry from B870 may

453   give an indication that the injection was a success, but the resistivity indicates that the oxidizing

454   agent barely reached the area with highest contamination at elevation 2.3 m. To get a similar level

455   of detail would have required a greatly increased number of monitoring wells and filters. The

456   permeability estimates from the measurements prior to the injection corroborate the story. The

457   area with high contamination where the oxidizing agent did *not* go, has a lower estimated

458   permeability than the area below, making it more preferable for the oxidizing agent to flow

459   beneath it during injection.

460   When comparing water conductivity measurements with the resistivity sections in figure 4 and 5,

461   we assume a constant, uniform formation factor, while the actual formation factors are unknown.

462   This obviously adds uncertainty to the water conductivity estimates, but independent estimates of

463   formation factors would again decrease this uncertainty.

464   The IP-derived permeability estimations show a good alignment between high and low

465   permeability areas and the geological transition from fine to coarse-grained sands, which is a

466   possible explanation for the spatial spreading of the injectants imaged through the time-lapse

467   inversions. Bias in the permeability estimation, especially on a quantitative level, might be present

468   because of high levels of contamination and the empirical nature of equation (3b). The resulting

469   permeability values are thus uncertain, but the relative variations are likely reasonable.

470   Unfortunately, we do not have any permeability estimates from other means, such as slug test, or

471   derived from grain size distributions in the test area. Furthermore, slugtests in B870 or B809

472 would yield information about the average permeability in the filters, instead of direct information

473 about the low permeability zone.

474 The resistivity sections in the non-injection rounds show high values in the unsaturated zone and

475 lower values below the groundwater table. The stripe-like structures observed in the resistivity

476 sections were initially thought to be inversion artifacts, but their consistency and visibility in data

477 increase our confidence in them. These structures may stem from geology, chemistry, or a

478 combination of both. The low resistivity around elevation 2-3 m is coinciding with a layer of fine-

479 grained sands and high contamination levels. The low resistivity levels could be the effect of

480 degradation products of PCE, trapped within the fine-grained sediments.

481 Prior to this study, it was not known how much the contamination would affect the resistivity in

482 the area. Christensen and Halkjær (2014) indicate that the general resistivity of the area was

483 unaffected above an elevation of -10 m, which is nearly 7 m below the targeted volume of this

484 survey. This is not in contradiction to our findings, as the majority of the volume appear to have

485 high, undisturbed resistivities, while some localized areas may have lower resistivity, possibly

486 due to contamination.

487 The extent and range of the injected oxidizing agent was tracked using the resistivity data alone

488 in time-lapse, but the permeability estimation obtained before the remediation, can be used to

489 predict the injectant spread pattern and to tailor the injection accordingly. However, during the

490 injection rounds, the IP-signal was severely affected by the conductive oxidizing agent, and signal

491 levels fell below the noise level for a majority of decays, so only IP data from the non-injectant

492 rounds was worth considering. For applications as the one presented in this study, and similar

493 hardware/current values, IP collection in injections rounds may be cancelled for the benefit of

494 faster acquisition time (and less frustration in the data processing). It has the added benefit that

495 all measurements may be closer in time, and closer to the injection event.

During the measurements in May and June (round 2 and round 3), about 30% fewer quadrupoles were measured, as the contact resistances were too high. No steps were taken however to resolve this issue in this study, as prior experience detailed in Bording, et al. (2019) showed that adding saltwater, while decreasing the contact resistance can increase borehole effects. As the main area of interest was in the saturated zone, where electrode contact resistances were low, this reduction in data was accepted. During fall and winter, precipitation increased resulting in lower contact resistances for the remaining rounds.

In this study, we have neglected effects arising from temperature variations between measurement rounds. The limited temperature information shows little variation (1-2 ºC, Table 2), so such effects are expected to be small.

In the recent past, the transition towards 3D inversions has been clear, but we have chosen to use 2D inversions in this study. This allowed us, within the same inversion code framework, to perform focused time-lapse inversions of resistivity and the spectral IP inversions, used for permeability estimation. The choice of 2D inversion comes with the problem of dealing with potential 3D effects. Some of such effects may be local conductive plumes in the xy plane with underestimated conductivity, and/or resistivity features outside the profile projected into the profile (Nimmer et al., 2008). Borehole effects resulting in resistivity contrast directly around the boreholes are expected to be limited as electrodes were installed using direct push, with a subsequent collapse of the sandy formation around the borehole electrodes. In the unsaturated zone, this collapse is however not guaranteed. Acknowledging the limitations of 2D inversions, but also the benefits of the time-lapse focusing scheme and of the full-decay IP inversion used in this study, work on a 3D code is currently in progress within our group (Madsen et al., 2019).

Conclusion

Resistivity and full waveform TDIP measurements were carried out in a cross-borehole setup at an active remediation site over the course of a year in order to test their capability in tracking the

521 spread of the injected oxidizing agent within the target volume. The collected resistivity data were

522 inverted with time-lapse focusing, while the IP data collected prior to injection were inverted in

523 terms of the MPA Cole-Cole re-parameterization, and subsequently used to estimate permeability

524 through petrophysical relations derived in the laboratory for unconsolidated samples. The

525 abovementioned setup, processing and inversion methods allowed for a spatial coverage of the

526 injection material not achievable by means of monitoring wells, and revealed the injected

527 oxidizing agent did spread in the majority of the saturated zone, but that local areas were not

528 reached by the injectant. This was unclear from the monitoring wells, but was identified easily

529 and clearly in the resistivity sections from the time-lapse inversions, which clearly visualized

530 where resistivity changes had occurred, and thus the extent of injected oxidizing agent. A

531 comparison between permeability estimations from the IP inversions and the spread of the

532 oxidizing agent furthermore showed, that the oxidizing agent did not spread in the predicted zones

533 of low permeability indicating that the first injection round may have had limited effect in terms

534 of remediation.

535 As a conclusion, we find that cross-borehole resistivity and TDIP measurements are a powerful

536 tool for mapping remediation material in the saturated zone when used in conjunction with other

537 direct investigation methods, with significant increase in area coverage as compared to the

538 traditional method of monitoring wells. Although the permeability estimates were not used to plan

539 the injection strategy in this study, the application of prior knowledge of the permeability field in

540 the planning phase may lead to more efficient and successful remediations.

541 Conflict of interest statement

542 The authors have no conflicts of interest to declare.

543

References

544

Arbejdsgruppen vedrørende Kærgård Plantage, 2005. Redegørelse vedrørende: Forureningen i Kærgård Plantage.

Arbejdsgruppen vedrørende Kærgård Plantage, 2006. Samlerapport.

Auken, E., Christiansen, A.V., Fiandaca, G., Schamper, C., Behroozmand, A.A., Binley, A., Nielsen, E., Effersø, F., Christensen, N.B., Sørensen, K.I., Foged, N., Vignoli, G., 2015. An overview of a highly versatile forward and stable inverse algorithm for airborne, ground-based and borehole electromagnetic and electric data. Exploration Geophysics 2015, 223-235.

Binley, A., Cassiani, G., Middleton, R., Winship, P., 2002. Vadose zone flow model parameterisation using cross-borehole radar and resistivity imaging. Journal of Hydrology 267, 147-159.

Binley, A., Keery, J., Slater, L., Barrash, W., Cardiff, M., 2016. The hydrogeologic information in cross-borehole complex conductivity data from an unconsolidated conglomeratic sedimentary aquifer. Geophysics 81, E409-E421.

Bording, T.S., Fiandaca, G., Maurya, P.K., Auken, E., Christiansen, A.V., Tuxen, N., Klint, K.E.S., Larsen, T.H., 2019. Cross-borehole tomography with full-decay spectral time-domain induced polarization for mapping of potential contaminant flow-paths. Journal of Contaminant Hydrology 226, 103523.

Chen, J., Hubbard, S.S., Williams, K.H., Orozco, A.F., Kemna, A., 2012. Estimating the spatiotemporal distribution of geochemical parameters associated with biostimulation using spectral induced polarization data and hierarchical Bayesian models. Water Resour. Res 48, 1-25.

Christensen, N.B., Halkjær, M., 2014. Mapping pollution and coastal hydrogeology with helicopterborne transient electromagnetic measurements. Exploration Geophysics 45, 243-254.

Cole, K.S., Cole, R.H., 1941. Dispersion and absorption in dielectrics. Journal of Chemical Physics 9, 341-351.

Commer, M., Newman, G.A., Williams, K.H., Hubbard, S.S., 2011. 3D induced-polarization data inversion for complex resistivity. Geophysics.

Doetsch, J., Fiandaca, G., Auken, E., Christiansen, A.V., Cahill, A.G., Jacobsen, J.D., 2015a. Field scale time-domain spectral induced polarization monitoring of geochemical changes induced by injected CO_2 in a shallow aquifer. Geophysics 80, WA113-WA126.

Doetsch, J., Ingemann-Nielsen, T., Christiansen, A.V., Fiandaca, G., Auken, E., Elberling, B., 2015b. Direct current (DC) resistivity and induced polarization (IP) monitoring of active layer dynamics at high temporal resolution. Cold Regions Science and Technology 119, 16-28.

Fiandaca, G., Doetsch, J., Vignoli, G., Auken, E., 2015. Generalized focusing of time-lapse changes with applications to direct current and time-domain induced polarization inversions. Geophysical Journal International 203, 1101-1112.

Fiandaca, G., Madsen, L.M., Maurya, P.K., 2018a. Re-parameterizations of the Cole-Cole model for improved spectral inversion of induced polarization data. Near Surface Geophysics 16, 385-399.

Fiandaca, G., Maurya, P.K., Balbarini, N., Hoerdt, A., Christiansen, A.V., Foged, N., Bjerg, P.L., Auken, E., 2018b. Permeability Estimation Directly From Logging-While-Drilling Induced Polarization Data. Water Resources Research 54, 2851-2870.

Fiandaca, G., Maurya, P.K., Balbarini, N., Hördt, A., Christiansen, A.V., Foged, N., Bjerg, P.L., Auken, E., 2018c. Permeability Estimation Directly From Logging-While-Drilling Induced Polarization Data. Water Resources Research 54, 2851-2870.

591   Fiandaca, G., Ramm, J., Binley, A., Gazoty, A., Christiansen, A.V., Auken, E., 2013. Resolving
592   spectral information from time domain induced polarization data through 2-D inversion.
593   Geophysical Journal International 192, 631-646.
594   Flores Orozco, A., Micić, V., Bücker, M., Gallistl, J., Hofmann, T., Nguyen, F., 2019. Complex-
595   conductivity monitoring to delineate aquifer pore clogging during nanoparticles injection.
596   Geophysical Journal International 218, 1838-1852.
597   Flores Orozco, A.n., Velimirovic, M., Tosco, T., Kemna, A., Sapion, H., Klaas, N., Sethi, R.,
598   Bastiaens, L., 2015. Monitoring the injection of microscale zerovalent iron particles for
599   groundwater remediation by means of complex electrical conductivity imaging. Environmental
600   science & technology 49, 5593-5600.
601   Gazoty, A., Fiandaca, G., Pedersen, J., Auken, E., Christiansen, A.V., 2012a. Mapping of landfills
602   using time-domain spectral induced polarization data: The Eskelund case study. Near Surface
603   Geophysics 10, 575-586.
604   Gazoty, A., Fiandaca, G., Pedersen, J., Auken, E., Christiansen, A.V., Pedersen, J.K., 2012b.
605   Application of time domain induced polarization to the mapping of lithotypes in a landfill site.
606   HESS 16, 1793-1804.
607   Günther, T., Rücker, C., 2012. Boundless electrical resistivity tomography (BERT) v. 2.0 open
608   access software for advanced and flexible imaging. C. Herve, A. Adler, and B. Lionhart, eds 100,
609   177-180.
610   Johansson, S., Fiandaca, G., Dahlin, T., 2015. Influence of non-aqueous phase liquid
611   configuration on induced polarization parameters: Conceptual models applied to a time-
612   domain field case study. Journal of Applied Geophysics 123, 295-309.
613   Karaoulis, M., Revil, A., Tsourlos, P., I, Werkema, D.D., Minsley, B.J., 2013. IP4DI: A software for
614   time-lapse 2D/3D DCresistivity and induced polarization tomography. Computers &
615   Geosciences.
616   Kemna, A., Binley, A., Slater, L., 2004. Crosshole IP imaging for engineering and environmental
617   applications. Geophysics 69, 97-107.
618   LaBrecque, D., Ramirez, A., Daily, W., Binley, A.M., Schima, S., 1996. ERT monitoring of
619   environmental remediation processes. Measurement Science and Technology 7, 375.
620   Loke, M.H., Dahlin, T., Rucker, D.F., 2014. Smoothness-constrained time-lapse inversion of data
621   from 3D resistivity surveys. Near Surface Geophysics 12, 5-24.
622   Looms, M.C., Binley, A., Jensen, K.H., Nielsen, L., Hansen, T.M., 2008a. Identifying unsaturated
623   hydraulic parameters using an integrated data fusion approach on cross-borehole geophysical
624   data. Vadose Zone Journal 7, 238-248.
625   Looms, M.C., Jensen, K.H., Binley, A., Nielsen, L., 2008b. Monitoring unsaturated flow and
626   transport using cross-borehole geophysical methods. Vadose zone journal 7, 227-237.
627   Madsen, L.M., Fiandaca, G., Auken, E., 2019. An Algorithm for 3D Modelling of Direct Current
628   Resistivity and Full-Response Time-Domain Induced Polarization Data, 25th European Meeting
629   of Environmental and Engineering Geophysics. European Association of Geoscientists &
630   Engineers, pp. 1-5.
631   Madsen, L.M., Fiandaca, G., Auken, E., Christiansen, A.V., 2017. Time-domain induced
632   polarization – an analysis of Cole–Cole parameter resolution and correlation using Markov
633   Chain Monte Carlo inversion. Geophysical Journal International 211, 1341-1353.
634   Mao, D., Lu, L., Revil, A., Zuo, Y., Hinton, J., Ren, Z.J., 2016. Geophysical monitoring of
635   hydrocarbon-contaminated soils remediated with a bioelectrochemical system. Environmental
636   science & technology 50, 8205-8213.
637   Mao, D., Revil, A., Hort, R.D., Munakata-Marr, J., Atekwana, E.A., Kulessa, B., 2015. Resistivity
638   and self-potential tomography applied to groundwater remediation and contaminant plumes:
639   Sandbox and field experiments. Journal of Hydrology 530, 1-14.

Maurya, P.K., Balbarini, N., Møller, I., Rønde, V., Christiansen, A.V., Bjerg, P.L., Auken, E., Fiandaca, G., 2018a. Subsurface imaging of water electrical conductivity, hydraulic permeability and lithology at contaminated sites by induced polarization. Geophysical Journal International, 770 - 785.

Maurya, P.K., Fiandaca, G., Christiansen, A.V., Auken, E., 2018b. Field-scale comparison of frequency- and time-domain spectral induced polarization. Geophysical Journal International 214, 1441-1466.

Nimmer, R.E., Osiensky, J.L., Binley, A.M., Williams, B.C., 2008. Three-dimensional effects causing artifacts in two-dimensional, cross-borehole, electrical imaging. Journal of Hydrology 359, 59-70.

Nivorlis, A., Dahlin, T., Rossi, M., Höglund, N., Sparrenbom, C., 2019. Multidisciplinary Characterization of Chlorinated Solvents Contamination and In-Situ Remediation with the Use of the Direct Current Resistivity and Time-Domain Induced Polarization Tomography. Geosciences 9, 487.

Olsson, P.-I., Fiandaca, G., Larsen, J.J., Dahlin, T., Auken, E., 2016. Doubling the spectrum of time-domain induced polarization by harmonic de-noising, drift correction, spike removal, tapered gating, and data uncertainty estimation. Geophysical Journal International.

Olsson, P.I., Dahlin, T., Fiandaca, G., Auken, E., 2015. Measuring time-domain spectral induced polarization in the on-time:decreasing acquisition time and increasing signal-to-noise ratio. Journal of Applied Geophysics 2015, 6.

Orozco, A.F., Williams, K.H., Kemna, A., 2013. Time-lapse spectral induced polarization imaging of stimulated uranium bioremediation. Near Surface Geophysics 11, 531-544.

Orozco, A.F., Williams, K.H., Long, P.E., Hubbard, S.S., Kemna, A., 2011. Using complex resistivity imaging to infer biogeochemical processes associated with bioremediation of an uranium-contaminated aquifer. Journal of Geophysical Research: Biogeosciences 116, G03001.

Pac, T.J., Baldock, J., Brodie, B., Byrd, J., Gil, B., Morris, K.A., Nelson, D., Parikh, J., Santos, P., Singer, M., Thomas, A., 2019. In situ chemical oxidation: Lessons learned at multiple sites. Remediation Journal 29, 75-91.

Pelton, W.H., Ward, S.H., Hallof, P.G., Sill, W.R., Nelson, P.H., 1978. Mineral discrimination and removal of inductive coupling with multifrequency IP. Geophysics 43, 588-609.

Perri, M.T., Cassiani, G., Gervasio, I., Deiana, R., Binley, A., 2012. A saline tracer test monitored via both surface and cross-borehole electrical resistivity tomography: Comparison of time-lapse results. Journal of Applied Geophysics 79, 6-16.

Rossi, M., Olsson, P.I., Johanson, S., Fiandaca, G., Bergdahl, D.P., Dahlin, T., 2017. Mapping geological structures in bedrock via large-scale direct current resistivity and time-domain induced polarization tomography. Near Surface Geophysics 15, 657-667.

Slater, L., Binley, A., 2003. Evaluation of permeable reactive barrier (PRB) integrity using electrical imaging methods. Geophys 68, 911-921.

Slater, L., Binley, A., 2006a. Engineered barriers for pollutant containment and remediation. Applied Hydrogeophysics 71, 293-317.

Slater, L., Binley, A., 2006b. Synthetic and field-based electrical imaging of a zerovalent iron barrier: Implications for monitoring long-term barrier performance. GEOPHYSICS 71, B129-B137.

Slater, L., Binley, A.M., Daily, W., Johnson, R., 2000. Cross-hole electrical imaging of a controlled saline tracer injection. Journal of Applied Geophysics 44, 85-102.

Tsitonaki, A., Petri, B., Crimi, M., MosbÆK, H., Siegrist, R.L., Bjerg, P.L., 2010. In Situ Chemical Oxidation of Contaminated Soil and Groundwater Using Persulfate: A Review. Critical Reviews in Environmental Science and Technology 40, 55-91.

Van Voorhis, G.D., Nelson, P.H., Drake, T.L., 1973. Complex resistivity spectra of porphyry copper mineralization. Geophysics 38, 49-60.

690 Weller, A., Slater, L., Binley, A., Nordsiek, S., Xu, S., 2015. Permeability prediction based on
691 induced polarization: Insights from measurements on sandstone and unconsolidated samples
692 spanning a wide permeability range. Geophysics 80, D161-D173.
693 Wemegah, D.D., Fiandaca, G., Auken, E., Menyeh, A., Danuor, S.K., 2017. Spectral time-domain
694 induced polarisation and magnetic surveying– an efficient tool for characterisation of solid
695 waste deposits in developing countries. Near Surface Geophysics 15, 75-84.

696

697

Tables

699 Table 1

700 Timing of injections and measurements, as well as the range of measured quadrupoles for the
701 ten measured configurations.

702

Activity	Date	# Quadrupoles per 3-borehole configuration
7-8 February 2018	Installation of electrodes	-
8-9 March 2018	1st measurement round	2026-2287
7-8 May 2018	2nd measurement round	1629-1708
5-6 June 2018	1st injection round	-
6-7 June 2018	3rd measurement round	1681-1860
26-27 September 2018	4th measurement round	2205-2575
29-30 October 2018	2nd injection round	-
30-31 October 2018	5th measurement round	2216-2575
14-15 March 2019	6th measurement round	2157-2575

703

704 Table 2

705 Water chemistry from water samples. Injection rounds marked with grey. nm denotes values not
706 measured.

707

Filter	Date yy-mm-dd	Interval masl [m]	pH -	EC µS/cm	Redox mV	Temp. °C	PCE µg/L	Sum (C6H6-C35) µg/L
B870-1	2018-05-30	1.3-(-0.2)	nm.	nm.	nm.	nm.	1700	4800
B870-1	2018-06-06	1.3-(-0.2)	1.7	20100	556	12.0	nm.	nm.
B870-1	2018-09-05	1.3-(-0.2)	4.7	402	-58	12.0	490	830
B870-2	2018-05-30	2.8-1.3	nm.	nm.	nm.	nm.	13000	15000
B870-2	2018-06-06	2.8-1.3	3.1	3190	540	12.5	nm.	nm.
B870-2	2018-09-05	2.8-1.3	4.6	473	-98	13.1	26000	23000
B809-3	2017	2.8-(-1.2)	nm.	nm.	nm.	nm.	23000	14000
B809-3	2018-06-06	2.8-(-1.2)	3.5	7100	539	10.9	nm.	nm.
B809-3	2018-09-06	2.8-(-1.2)	4.6	405	-50	11.9	nm.	nm.

708

709

710 Table 3

711 Soil samples from B809. bd. is below detection, and nm. is not analyzed.

| Sample depth | 2017 Baseline | | After second injection round | |
	PCE	Sum (C6H6-C35)	PCE	Sum (C6H6-C35)
masl [m]	mg/kg	mg/kg	mg/kg	mg/kg
2.8	15	20	860	820
2.3	16000	7700	510	390
1.8	320	42	190	12
1.3	81	1.6	bd.	0.8
0.8	220	240	bd.	0.22
0.3	bd.	1.7	bd.	0.043
-0.2	bd.	0.98	bd.	0.058
-0.7	89	90	nm.	nm.
-1.2	bd.	1.3	nm.	nm.
-1.7	bd.	0.18	nm.	nm.
-2.2	bd.	0.5	nm.	nm.

712

713

714
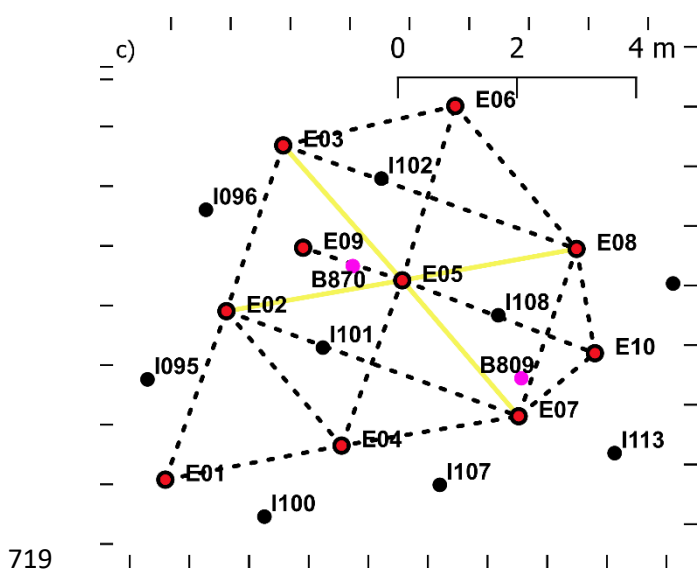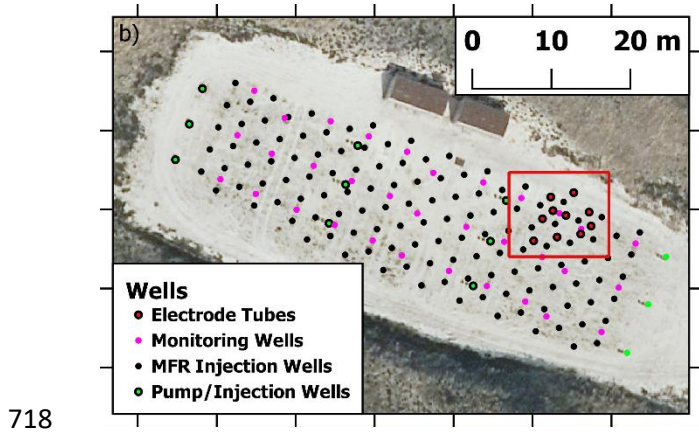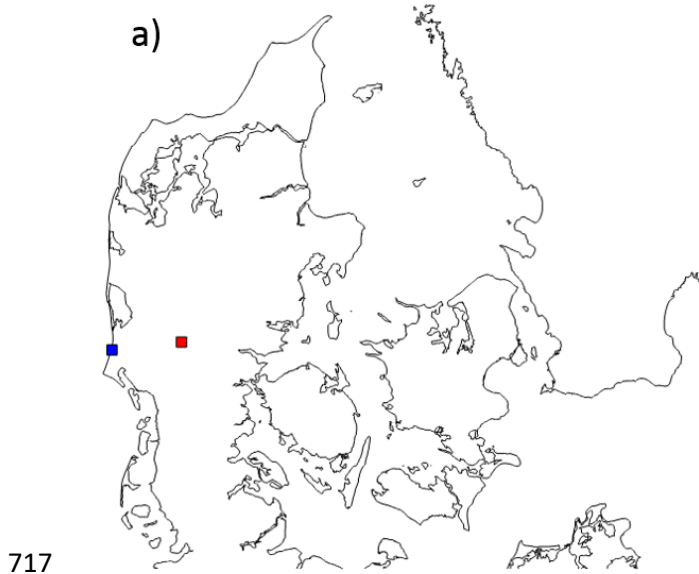
Figures

Figure 1

720   **Figure 1. a) Location of the survey site Kaergaard Plantation in blue, and**
721   **Grindstedværket in red. b) Overview of pit 3. c) Close up of the used electrode tubes, the**
722   **lines denote the measured configurations, the configurations presented in this paper are in**
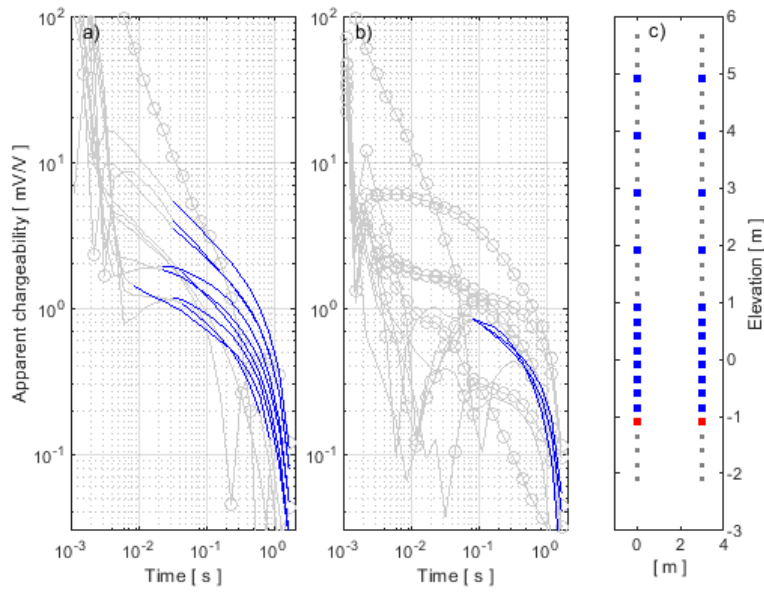723   **yellow.**
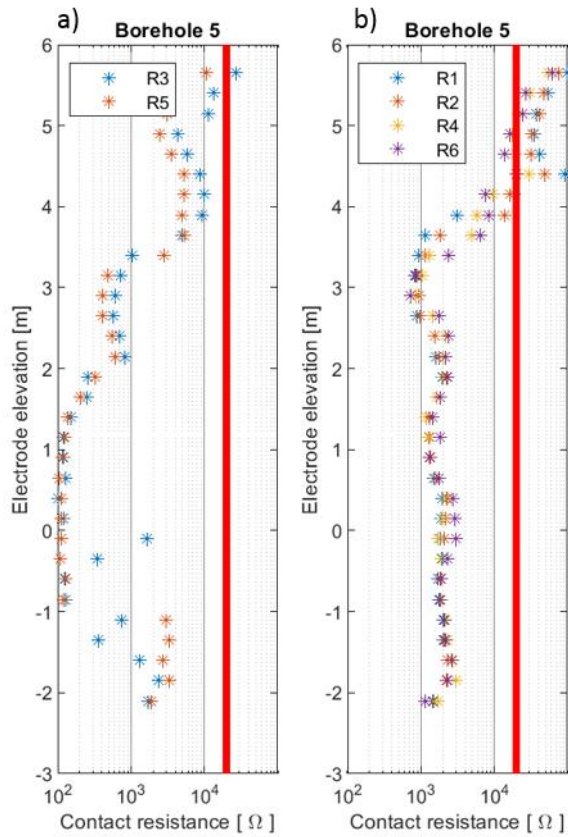
Figure 2. Contact resistances measured in borehole 5. a) Contact resistances for the injection rounds. b) Contact resistances of the non-injection rounds. The red line shows the cutoff criteria used for no-contact electrodes.

730   Figure 3

731

Figure 3. Selected IP data from profile E03-E05-E07. a) Round 1, used for IP inversions.
b) Round 3, immediately after injection, kept data shown with blue lines, discarded data
shown with grey lines, and negative data marked with circles. c) Positions of electrodes,
current electrodes marked with red, potential electrodes marked with blue, other
electrodes in grey. Potentials were measured in pairs of electrodes with same elevation.

738 Figure 4
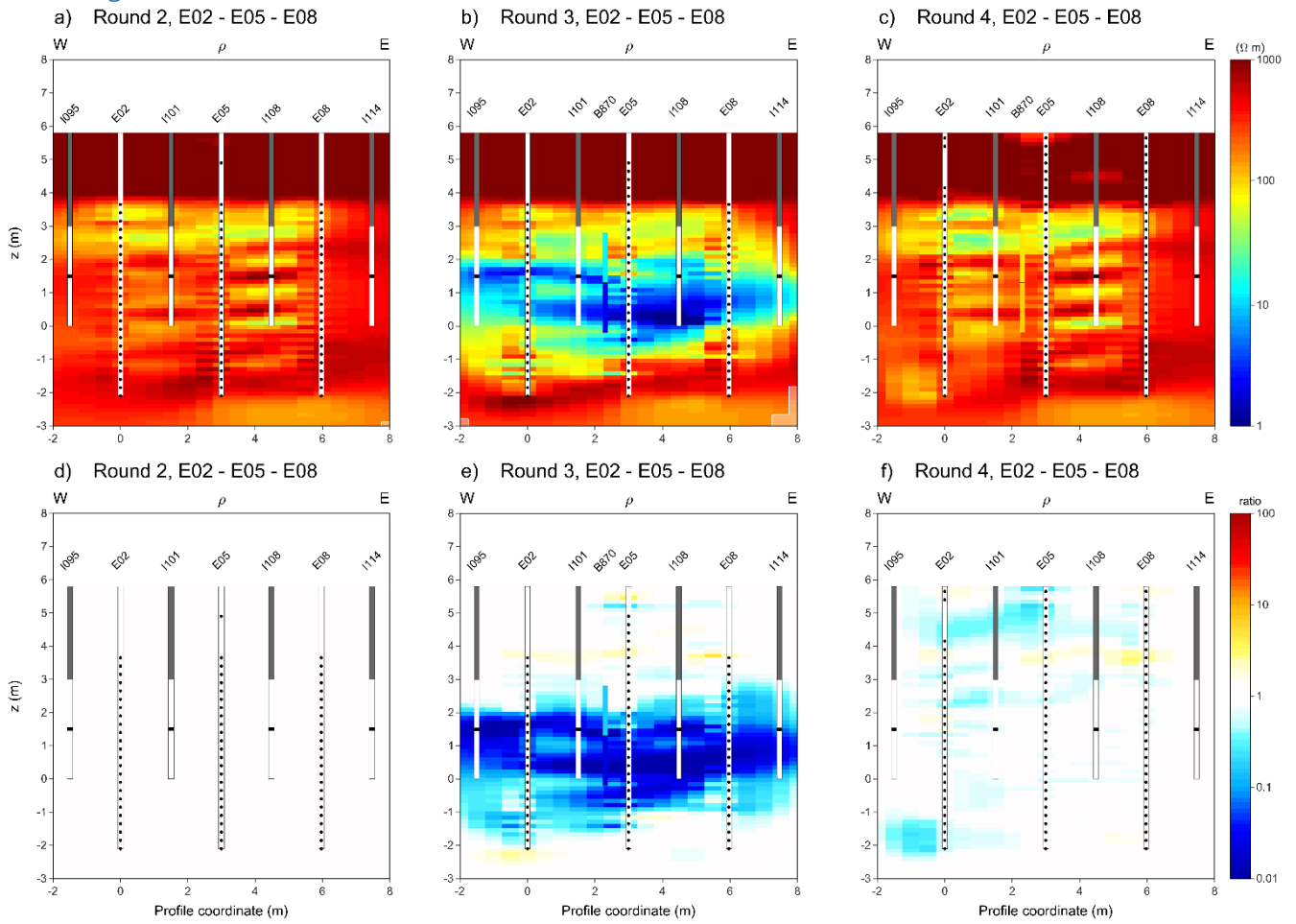
Figure 4. Time-lapse inversion results for configuration E02-E05-E08, rounds 2-4 against round 1. a)-c) Resistivity sections for round 2-4, respectively. d)-f) Ratio-plots of resistivity rounds 2-4 against round 1. Water EC converted to resistivity plotted in b) and c). Ratio of water EC between round 3 and 4 plotted in e).
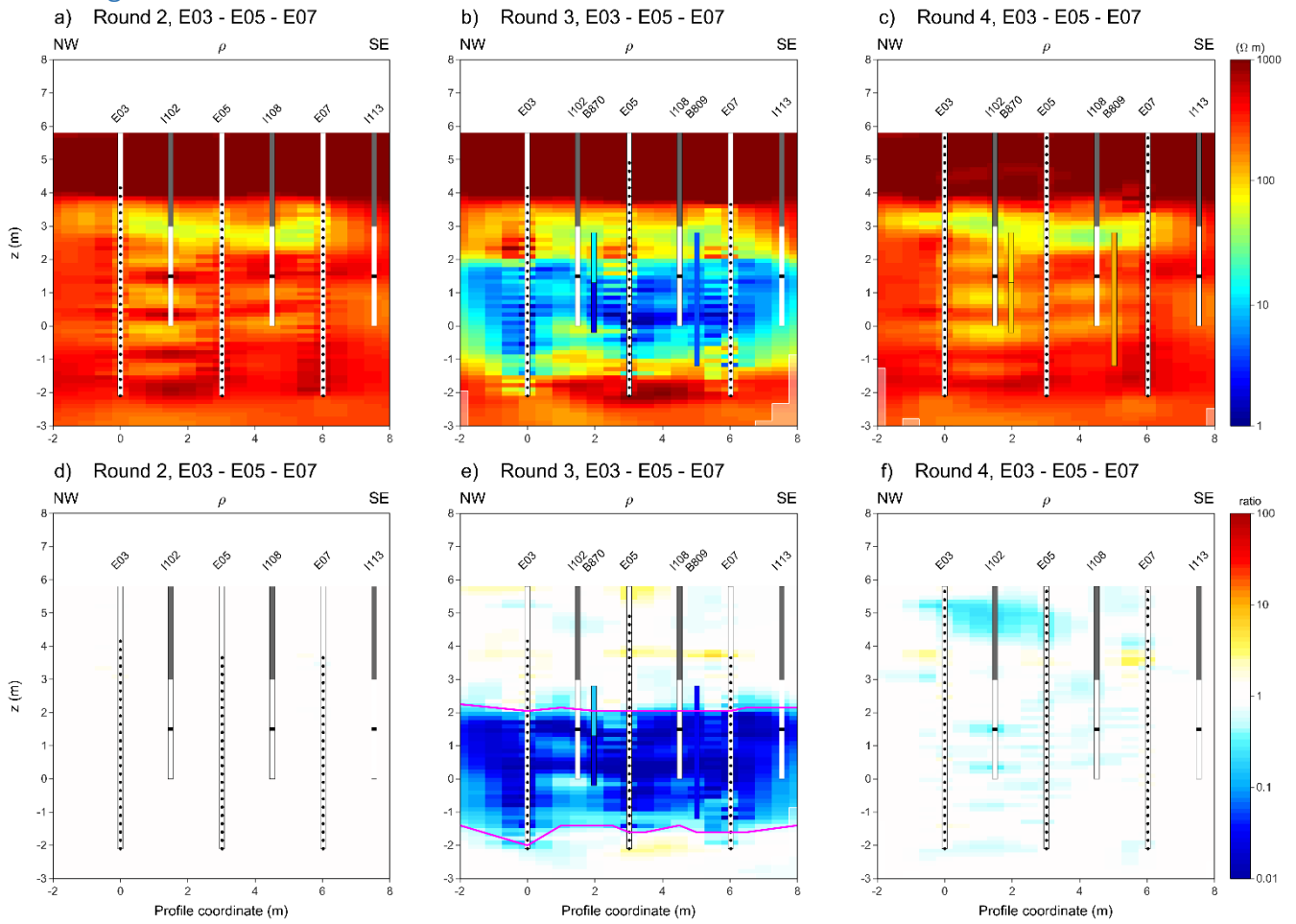
Figure 5

Figure 5. Time-lapse inversion results for configuration E03-E05-E07, rounds 2-4 against round 1. a)-c) Resistivity sections for round 2-4, respectively. d)-f) Ratio-plots of resistivity rounds 2-4 against round 1. Water EC converted to resistivity plotted in b) and c). Ratio of water EC between round 3 and 4 plotted in e).
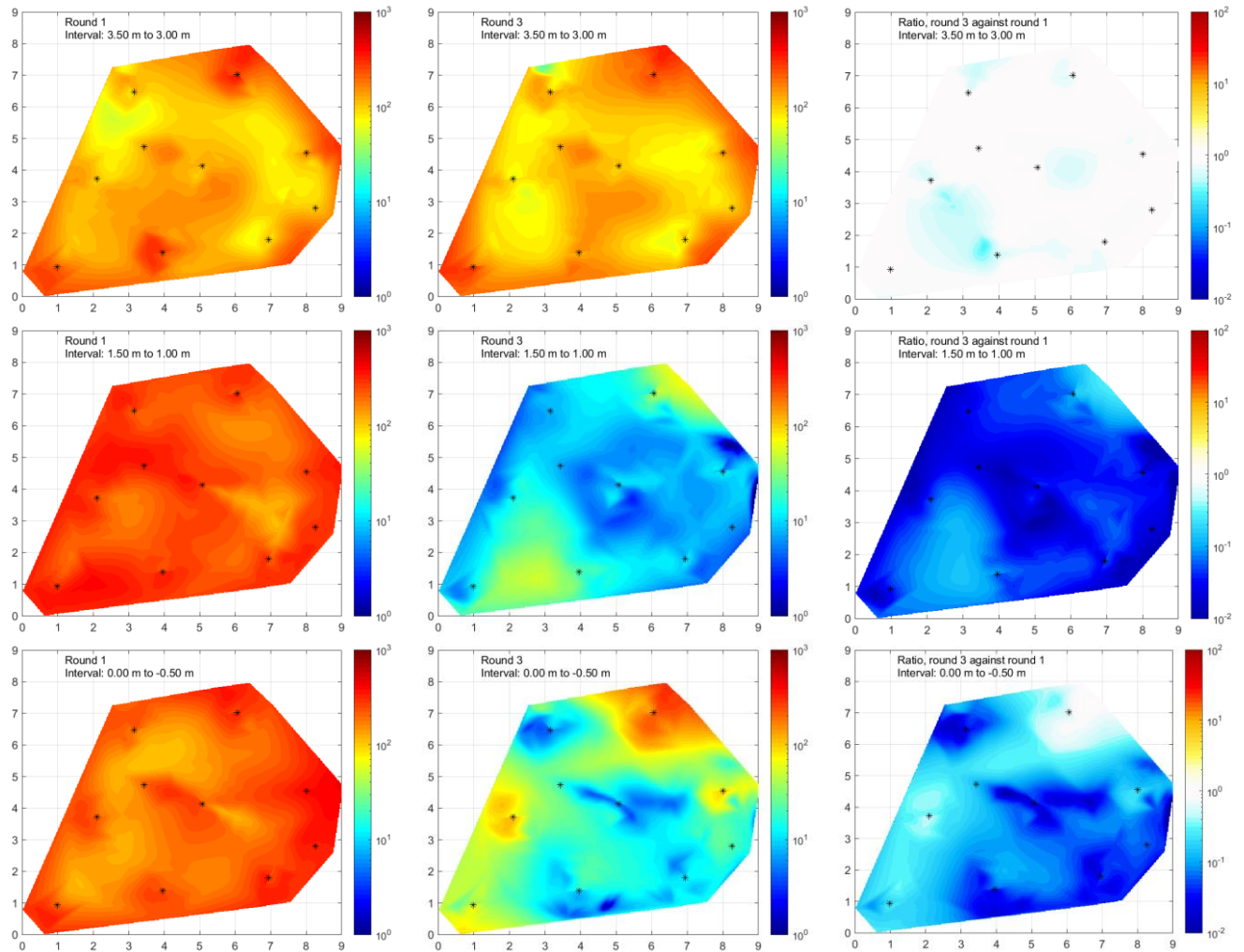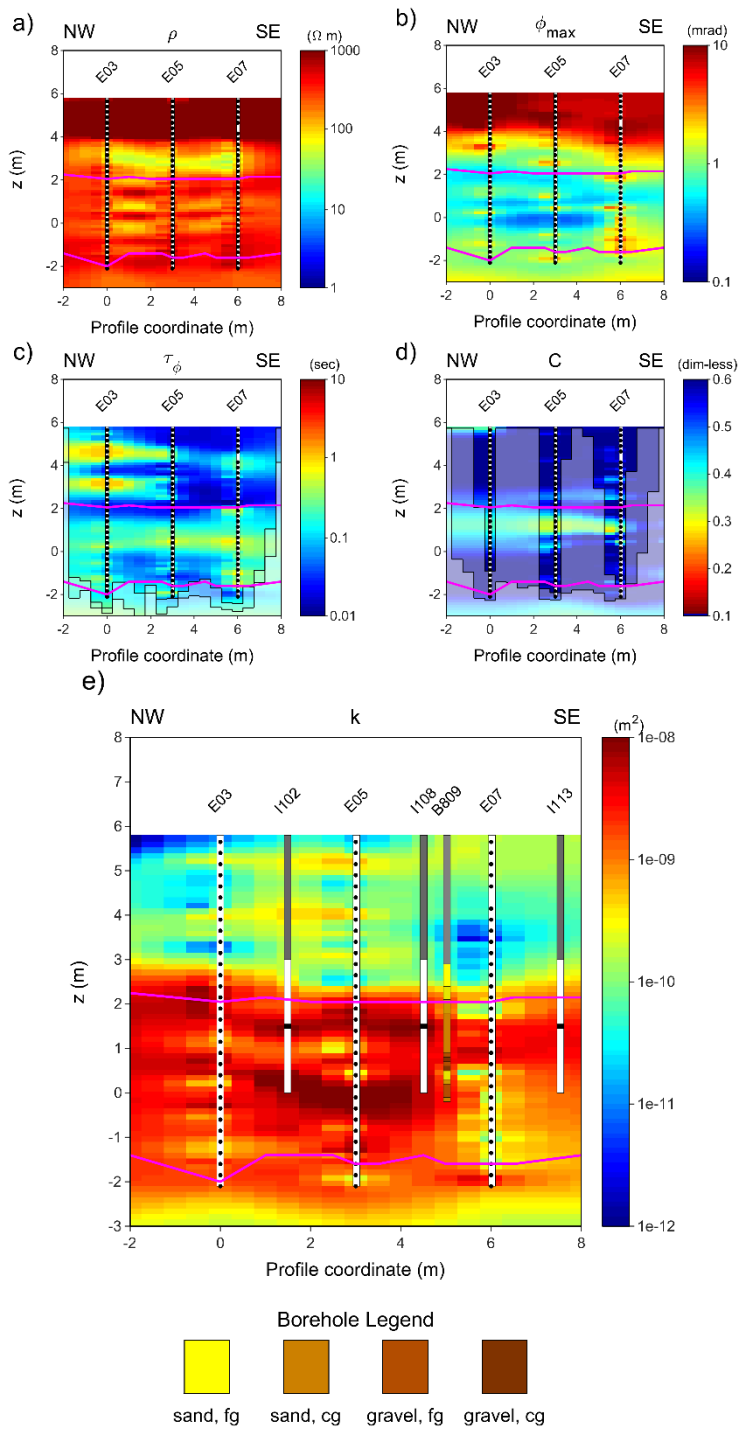
758   Figure 6

Figure 6. Mean interval resistivity maps round 1 and 3, and similarly, mean interval
resistivity ratio maps.

761

Figure 7

Figure 7. IP inversion results for configuration E03-E05-E07, round 1, with conductive contour overlay from Figure 4e. a) Resistivity section. b) ϕ_{max} section. c) τ_ϕ section. d) C section. e) Estimated permeability section with geology from B809.